FULL PAPER

Effect of projectile shape and interior structure on crater size in strength regime

T. Kadono[1*] , M. Arakawa[2], S. Tsujido[2], M. Yasui[2], S. Hasegawa[3], K. Kurosawa[4], K. Shirai[2], C. Okamoto[2], K. Ogawa[2,5], Y. Iijima[3], Y. Shimaki[3] and K. Wada[4]

Abstract

Experiments on crater formation in the strength regime were conducted using projectiles of various shapes with an aspect ratio of ~ 1, including both solid and hollow interiors. The surface diameter, inner (pit) diameter, and depth of the craters on basalt and porous gypsum targets were measured. Using the bulk density of the projectile, the surface diameter and depth for basalt and the pit diameter and depth for porous gypsum were scaled using the pi-scaling law for crater formation in the strength regime. The numerical code iSALE was used to simulate the impact of projectiles of various shapes and interior structure with similar bulk densities. Results show that the distributions of the maximum (peak) pressure experienced and particle velocity in the targets were similar regardless of projectile shape and interior structure, implying that the dimensions of the final craters were almost identical. This is consistent with the experimental results. Thus, we conclude that the size of the craters formed by the impact of projectiles with different shape and interior structure can be scaled using a conventional scaling law in the strength regime, using bulk density as projectile density.

Keywords: Hypervelocity impact, Crater formation, Strength regime, Hollow projectile, Scaling law

Graphical abstract
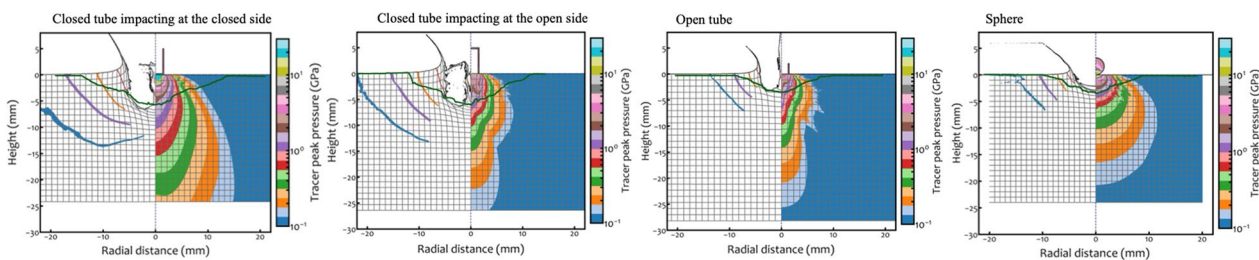
Introduction

An impact experiment was performed on the surface of the C-type asteroid 162173 Ryugu using an instrument called the Small Carry-on Impactor (SCI), carried by JAXA spacecraft Hayabusa2 (Arakawa et al. 2020). This SCI instrument launched a copper projectile with a mass of 2 kg, in the shape of a spherical shell—a hollow ball with a thickness of approximately 5 mm and a diameter of 13 cm. An important outcome is that the size of the artificial crater produced on Ryugu is well scaled by a conventional scaling law in the gravity regime when the bulk density is simply set as the projectile density in the
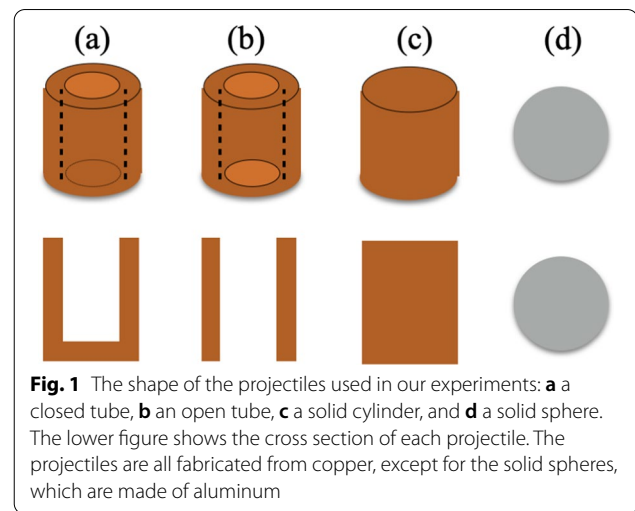
*Correspondence: kadono@med.uoeh-u.ac.jp

[1] Department of Basic Sciences, University of Occupational and Environmental Health, Kitakyushu, Japan
Full list of author information is available at the end of the article

Kadono *et al. Earth, Planets and Space*   (2022) 74:132

Page 2 of 12

scaling law (Arakawa et al. 2020), where the bulk density of the projectile 1.740 g/cm^3 is calculated by assuming that the projectile is a sphere with a diameter of 13 cm and a mass of 2 kg.

Projectiles with such complex structures, including hollow interior, have been used not only for Hayabusa2 but also for other planetary explorations in recent years, such as DEEP IMPACT (A'Hearn et al. 2005; Sugita et al. 2005; Kadono et al. 2007) and LCROSS (Colaprete et al. 2010; Schultz et al. 2010). However, to date, most impact experiments in laboratories have used solid projectiles, because the main purpose of these experiments has been simulating the impact of celestial bodies (e.g., Melosh 1989). Hence, there have been a limited number of experiments in the field or in laboratories using projectiles with complex structures, such as the impact of hollow aluminum and nylon projectiles into sand and pumice targets in the context of clustered impacts (Schultz and Gault 1985) and the calibration experiments for the SCI impact (Saiki et al. 2017) and the LCROSS impact (Hermalyn et al. 2012). In particular, there have been few impact experiments using complex-structured projectiles and targets with strength. The SCI projectile in the Hayabusa2 mission collided with smaller grains on the surface of Ryugu, but larger boulders than the SCI projectile exist near the impact point and it could have possibly collided with these boulders. Hence, the impact of projectiles with hollow interiors to larger boulders with strength could occur in future missions, and we should investigate the craters caused by projectiles with hollow interiors on targets with strength. Thus, in this study, we conducted impact experiments using projectiles of cylindrical or spherical shapes with hollow or solid interiors and targets with strength, basalt, and porous gypsum. In gravity regime, as shown in the impact of the SCI projectile, the crater efficiency of hollow projectiles can be scaled by the pi-scaling law for crater formation when the bulk density of the projectile is used (Schultz and Gault 1985). We investigated the sizes of the craters formed on the targets with strength to verify that, as in the gravity regime, crater size is scaled by a conventional scaling law when bulk density is set as projectile density. Numerical simulation is done to support the experimental results.

Experiment

We used four types of projectiles, as illustrated in Fig. 1: (a) a "closed" copper tube (one side is closed and the other is open), (b) an "open" copper tube (both sides are open), (c) a solid copper cylinder, and (d) a solid aluminum sphere. Tube-shaped projectiles were used because their thickness can be easily adjusted to match bulk density. The diameter, D_p, height, H, and bulk density, ρ_p, of the projectiles are listed in Table 1. The

Fig. 1 The shape of the projectiles used in our experiments: **a** a closed tube, **b** an open tube, **c** a solid cylinder, and **d** a solid sphere. The lower figure shows the cross section of each projectile. The projectiles are all fabricated from copper, except for the solid spheres, which are made of aluminum

projectile was accelerated with a split-type sabot using a two-stage hydrogen gas gun at Institute of Space and Astronautical Science (ISAS) of JAXA (Kawai et al. 2010). Open tubes impacted on one side, and the solid cylinders impacted on one flat surface. For closed-tube projectiles, we conducted our experiments in two different ways: impact from the closed side or impact from the open side. Targets were porous gypsum and basalt, which have been extensively used to investigate the crater formation process on asteroid surfaces with high porosity (e.g., Yasui et al. 2012) and lunar and terrestrial surfaces covered with volcanic materials (e.g., Gault and Heitowit 1963), respectively. The tensile strength of these materials, Y_t, was 2.52 MPa (Yasui et al. 2012) and 19.3 MPa (Nakamura et al. 2007), respectively. Target density, δ_t, is listed in Table 1. Impact velocity, V, was approximately 2−4 km/s. Seventeen shots were successful. The impact conditions are listed in Table 1.

After the shot, the target surface was scanned by a high-resolution three-dimensional geometry measurement system with a semi-conductor laser displacement sensor (COMS MAP-3D) at ISAS/JAXA. We obtained the topography of target surfaces every 0.2 mm interval. Based on this data, we determined the crater diameter and depth.
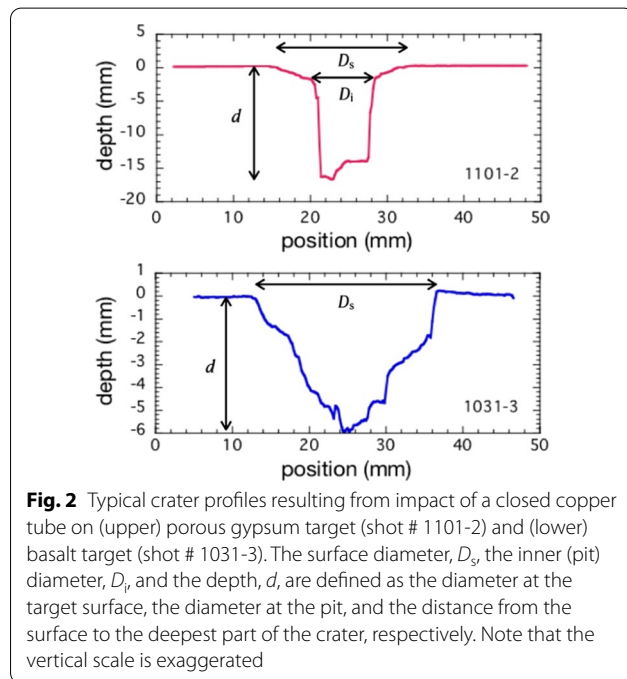
Results

Figure 2 shows typical crater profiles resulting from a closed copper tube impacting on porous gypsum (upper) and basalt (lower) targets. The craters on the porous gypsum targets consist of a deep pit with a spall region around the pit. We measured two kinds of diameters for the crater on the porous gypsum targets: the surface (spall) diameter D_s at the surface of the targets and the inner (pit) diameter D_i, respectively, as indicated in the

Kadono *et al. Earth, Planets and Space* (2022) 74:132

Page 3 of 12

Table 1 Experimental conditions and results

Shot #	Projectile	ρ_p (g/cm^3)	D_p (mm)	H (mm)	Target	δ_t (g/cm^3)	V (km/s)	D_s/D_p	D_i/D_p	d/D_p
1030–1	]	2.58	3.19	5.03	G	0.889	1.89	1.89	3.39	2.13	4.91
1030–2	[	2.63	3.17	5.01	G	0.860	1.82	2.26	1.84	3.34
1030-3	]	2.56	3.17	5.01	G	1.07	3.86	13.0	4.36	7.74
1031-1	[	2.57	3.19	5.02	G	1.07	3.88	11.2	3.90	8.08
1031-2	]	2.59	3.18	5.01	B	2.71	1.91	9.24	–	1.73
1031-3	[	2.62	3.18	5.01	B	2.73	1.90	7.77	–	1.84
1031-4	S	2.74	3.2	3.2	G	0.940	1.87	4.10	2.58	4.34
1031-5	S	2.74	3.2	3.2	B	2.73	1.92	6.21	–	1.06
1031-6	S	2.74	3.2	3.2	G	1.14	4.19	11.5	4.24	4.03
1101-1	C	8.84	3.0	1.65	G	0.880	1.79	5.53	2.89	8.38
1101-2	]	2.58	3.18	5.02	G	1.14	1.84	5.97	2.38	5.48
1101-3	]	2.58	3.18	5.02	G	0.843	4.05	3.39	2.13	4.91
0606-2	=	2.55	3.0	2.0	G	1.12	2.02	2.66	1.76	3.34
0606-3	=	2.55	3.0	2.0	G	0.936	2.09	1.86	1.86*	3.97
0606-4	C	8.84	2.0	1.3	G	0.928	1.90	2.81	2.81*	11.0
0925-1	=	2.59	3.0	2.0	B	2.67	1.82	5.30	–	1.04
0925–2	C	9.06	2.0	1.1	B	2.72	1.93	9.12	–	1.88

Projectile]: copper closed tube impacting at the closed side; [: copper closed tube impacting at the open side; =: copper open tube; S: aluminum solid sphere; C: copper solid cylinder

Target G: porous gypsum; B: basalt; *No spallation and we set $D_s = D_i$

Fig. 2 Typical crater profiles resulting from impact of a closed copper tube on (upper) porous gypsum target (shot # 1101-2) and (lower) basalt target (shot # 1031-3). The surface diameter, D_s, the inner (pit) diameter, D_i, and the depth, d, are defined as the diameter at the target surface, the diameter at the pit, and the distance from the surface to the deepest part of the crater, respectively. Note that the vertical scale is exaggerated

upper panel of Fig. 2. Shot numbers 0606-3 and 0606-4 were exceptions, as there was no clear spallation; therefore, only the diameter at the surface D_s was measured and set $D_s = D_i$. On the other hand, there were no clear pits in the craters on the basalt targets. Hence, we measured only the surface diameter of the crater on the basalt targets. We also measured the depth, d, of the crater, which was measured from the surface to the deepest part of the crater.

Figure 3 shows crater diameters and depth normalized by projectile diameter, D_p, (a) D_s/D_p, (b) D_i/D_p, and (c) d/D_p, as a function of ρ_p. For comparison, previous data obtained using cylindrical solid nylon projectiles and basalt targets (Dohi et al. 2012) and a spherical solid nylon projectile and a porous gypsum target (Yasui et al. 2012) are also plotted. There appears to be no systematic difference depending on projectile type, projectile orientation, or whether the projectile structure (i.e., solid or hollow). The values, D_s/D_p, D_i/D_p, and d/D_p, are listed in Table 1.

Discussion

Scaling by conventional crater scaling law

The pi-scaling law for crater size in the strength regime describes crater size, R, using the dimensionless parameters $\pi_R = R(\delta_t/m)^{1/3}$, $\pi_3 = (Y_t/\delta_t V^2)$, and $\pi_4 = (\delta_t/\delta_p)$ as

$$\pi_R = k_1 \pi_3^{-\mu/2} \pi_4^{(1-3\nu)/3}, \tag{1}$$

where δ_t, m, V, and δ_p are target density, projectile mass, impact velocity, and projectile density, respectively, and k_1, μ, and ν are empirical parameters related to the point source approximation and determined by laboratory

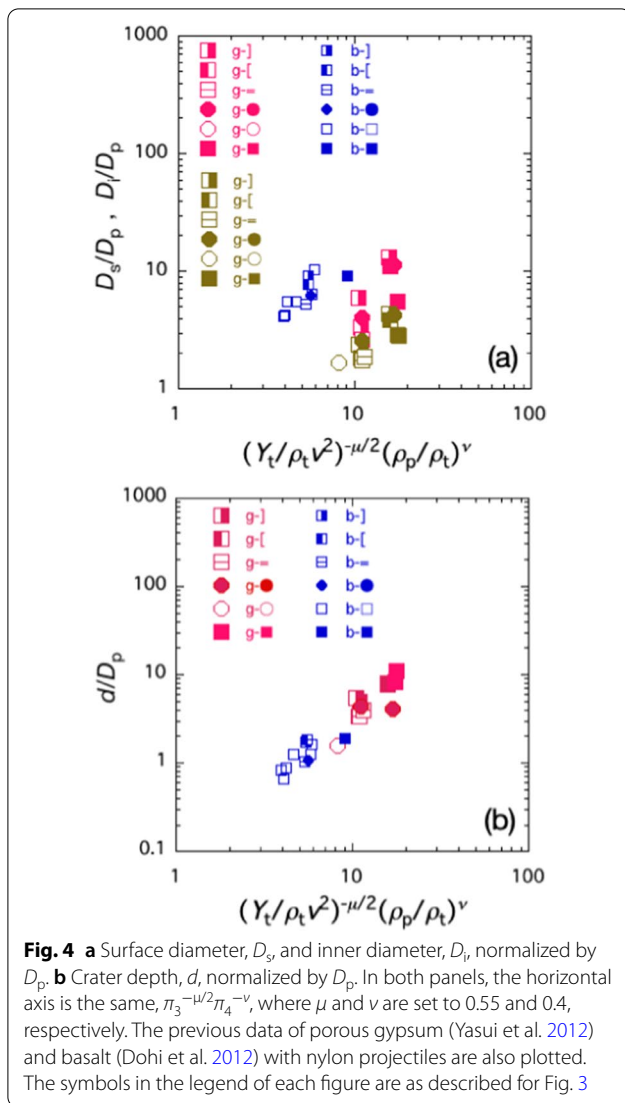Kadono *et al. Earth, Planets and Space*   (2022) 74:132

Page 4 of 12
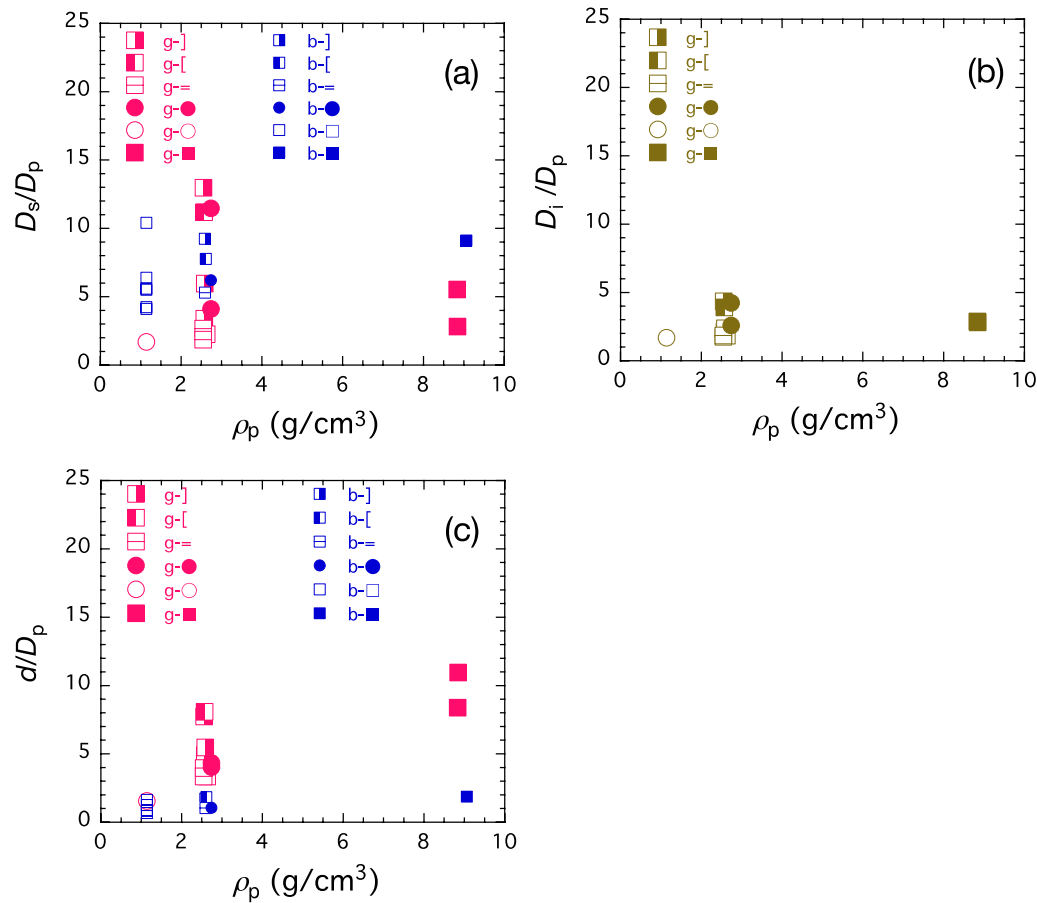
Fig. 3 Crater diameters (surface and inner) and depth normalized by projectile diameter, D_p, as a function of projectile bulk density, ρ_p, in g/cm³, **a** D_s/D_p, **b** D_{pi}/D_p, and **c** d/D_p. Symbols, "g-" and "b-", indicate porous gypsum and basalt targets, respectively. Projectile structures and orientations are also indicated; symbols "]", "[", "=", "filled black circle", and "filled black square" indicate the impact of closed tubes from the closed side, the impact of closed tubes from the open side, the impact of open tubes from one open side, the impact of solid spheres, and the impact of solid cylinders, respectively. Symbols "open circle" and "open square" indicate the previous results of the impact of a spherical nylon projectile onto a porous gypsum block (1 point; Yasui et al. 2012) and of cylindrical nylon projectiles onto basalt blocks (6 points; Dohi et al. 2012)

experiments (Housen and Holsapple 2011). Since $\pi_R \sim (R/D_p)\pi_4^{1/3}$, where D_p is the projectile diameter, Eq. (1) becomes

$$\left(\frac{R}{D_p}\right) \sim \left(\frac{\delta_p}{\delta_t}\right)^\nu \left(\frac{Y_t}{\delta_t V^2}\right)^{-\mu/2}. \qquad (2)$$

Figure 4 shows normalized crater size as a function of the right-hand side of Eq. (2). We set the empirical parameters, μ and ν, to typical values previously obtained for hard rocks of 0.55 and 0.4, respectively (Holsapple 1993; Housen and Holsapple 2011), and the projectile density δ_p to the bulk density of projectiles, ρ_p. Previous data are also plotted for basalt (Dohi et al. 2012) and porous gypsum (Yasui et al. 2012). For basalt targets, the data of surface diameter D_s/D_p in (a) and depth d/D_p in (b) are in good agreement with the previous data and

show a linear relationship. For porous gypsum, the data for the surface (spall) diameter D_s/D_p are scattered, but the data for inner (pit) diameter D_i/D_p and depth d/D_p appear to be linearly correlated and in good agreement with the previous data using different types of projectiles. Thus, even when projectiles have varied shapes, crater sizes in the strength regime can be scaled using a conventional scaling law previously established, using bulk density as ρ_p. Note that spallation in porous gypsum targets often produces large fragments (e.g., Fig. 3 in Suzuki et al. 2018). Such a process with large crack propagation is highly probabilistic; hence, the surface (spall) diameter D_s/D_p for porous gypsum may scatter. This may be the reason why spallation occurred in shot number 0606-2 but not in 0606-3, even though the impact conditions for these shots were almost the same. On the other hand, the

Kadono *et al. Earth, Planets and Space* (2022) 74:132

Page 5 of 12

Fig. 4 a Surface diameter, D_s, and inner diameter, D_i, normalized by D_p. **b** Crater depth, d, normalized by D_p. In both panels, the horizontal axis is the same, $\pi_3^{-\mu/2}\pi_4^{-\nu}$, where μ and ν are set to 0.55 and 0.4, respectively. The previous data of porous gypsum (Yasui et al. 2012) and basalt (Dohi et al. 2012) with nylon projectiles are also plotted. The symbols in the legend of each figure are as described for Fig. 3

1.7 MPa for the SB boulder (Kadono et al. 2020). In this case, if porous gypsum can simulate the boulders with high porosity on Ryugu, Fig. 4 indicates that D_i/D_p and d/D_p are ~ 1, respectively, suggesting that the crater is much smaller than the actual crater size that formed in the gravity regime, and would have been extremely difficult to find.

Numerical simulations

We investigated the crater formation process under the conditions experimented in this study using a general-purpose shock physics code, iSALE-2D (Wünnemann et al. 2006) to confirm the limited dependence of crater size on projectile shape. This code is an extension of the SALE code (Amsden et al. 1980), which is capable of modeling shock processes in geological materials (Melosh et al. 1992; Ivanov et al. 1997; Collins et al. 2004; Wünnemann et al. 2006).

Three types of projectiles were considered: closed copper tubes, open copper tubes, and solid aluminum spheres, corresponding to projectiles described in

Table 2 Input parameters of the material models for the metal projectiles

	Copper	Aluminum
EOS model	Tillotson EOS[a]	Tillotson EOS[a]
Poisson's ratio	0.34[b]	0.33[c]
Melting temperature (K)	1,356[d]	978[e]
Simon parameter *a* (GPa)	49.228[d]	7.98[e]
Simon parameter *c*	1.027[d]	0.57[e]
Specific heat (J/K/kg)	392.5[f]	896[f]
Johnson–Cook parameter *A* (MPa)	90[g]	244[h]
Johnson–Cook parameter *B* (MPa)	292[g]	488[h]
Johnson–Cook parameter *N*	0.31[g]	0.5[h]
Johnson–Cook parameter *C*	0.025[g]	0.0[h]
Johnson–Cook parameter *m*	1.09[g]	3[h]
Reference temperature (K)	293	293

Detailed descriptions of the parameters can be found in the iSALE manual (Collins et al. 2016)

[a] Tillotson (1962)

[b] Köster and Franz (1961)

[c] We used an aluminum alloy. The Poisson ratio was taken from the data compiled on the web page (http://asm.matweb.com/search/GetReference.asp?bassnum=ma6061t6) provided by ASM Aerospace Speciation Metals Inc. The database was constructed based on the information provided by the Aluminum Association Inc

[d] The pressure-dependent melting temperature of copper presented in Japel et al. (2005) was fitted by the Simon equation (e.gPoirier 1991; Wünnemann et al. 2008)

[e] Hänström and Lazor (2000)

[f] The Dulong–Petit values were used

[g] Johnson and Cook (1983)

[h] Pierazzo et al. (2008)

reason of no spallation in shot number 0606-4 would be different. The density ratio of projectile to target in shot number 0606-4 was very high ~ 9: such high density ratio generally causes a carrot-shaped crater without spallation (e.g., Love et al. 1993; Kadono et al. 2012). Furthermore, target differences cannot be scaled by only strength and density. Other parameters should be considered, but these are beyond the scope of this paper and are not discussed further.

As an application of our results, we consider the case if the SCI projectile collides with a boulder on Ryugu (e.g., "SB" boulder with a size of 5 m existing in the vicinity of the SCI impact point as shown in Arakawa et al. 2020). The left-hand side of Eq. (2) becomes ~ 6.6, when setting ρ_p and V to 1.74 g/cm^3 and 2 km/s for the SCI projectile (Arakawa et al. 2020) and ρ_t and Y_t to 1 g/cm^3 and

Kadono *et al. Earth, Planets and Space* (2022) 74:132

Page 6 of 12

Table 3 Material model parameters for basalt targets

	Basalt*
EOS model	ANEOS
Poisson's ratio	2.5
Melting temperature (K)	1360
Simon parameter *a* (GPa)	4.5
Simon parameter *c*	3.0
Thermal softening coefficient	0.7
Cohesion (intact) (MPa)	20
Frictional constant (intact)	1.4
Cohesion (damaged) (MPa)	0.01
Frictional constant (damaged)	0.6
Limiting strength (GPa)	2.5
Minimum failure strain	10^{-4}
Constant for the damage model	10^{-11}
Threshold pressure for the damage model (MPa)	300

*The parameters used in this study are the same as used in Bowling et al. (2020)

Table 4 Calculation settings

Parameters and settings*	Values
Computational geometry	Cylindrical coordinate
Number of computational cells in the *R* direction	2000
Number of computational cells in the *Z* direction	3000
Number of cells for the extension in the *R* direction	400
Number of cells for the extension in the *Z* direction	400
Extension factor	1.02
Grid spacing (m/grid)	10^{-5}
Artificial viscosity a_1	0.24
Artificial viscosity a_2	1.2
Impact velocity (km/s)	2.0
High-speed cutoff	Twofold impact velocity
Low-density cutoff (kg/m^3)	100

*Detailed descriptions of the parameters can be found in the iSALE manual (Collins et al. 2016)

Figs. 1a, b, and d, respectively. The diameter and height of all the projectiles were set to 3.2 mm. To simulate the impact of projectiles having a similar bulk density, the thicknesses of the closed and open tubes were set to 0.20 and 0.25 mm, respectively, resulting in the bulk densities of the closed and open tubes being 2.53 and 2.58 g/cm^3, respectively.

Four types of impacts were simulated: (a) a closed tube impacting on the closed side, (b) a closed tube impacting on the open side, (c) an open tube on one open side, and (d) a solid aluminum sphere. These projectiles collided perpendicularly on basaltic target flat surfaces along the central axis. Impact velocity was set at 2 km/s.

The calculation settings are summarized as follows: we used the two-dimensional version of iSALE, which is referred to as iSALE-Dellen (Collins et al. 2016) to simulate the vertical impacts performed in the experiments. We used the Tillotson equation of state (EOS) for copper and aluminum (Tillotson 1962) and the "Analytical" EOS (ANEOS) (Thompson and Lauson 1972) for basalt (Pierazzo et al. 2005; Sato et al. 2021). We also employed a constitutive model to calculate the elastoplastic behaviors of both shocked projectiles and targets. The Johnson–Cook model (Johnson and Cook 1983) was used for metal projectiles. We used the "ROCK" model implemented in the iSALE for the basalt target, which is a combination of the Drucker–Prager model (Drucker and Prager 1952) for damaged rocks and the Lundborg model for intact rocks (Lundborg 1968). The two models were coupled with a damage parameter ranging from 0 to 1, depending on the total plastic strain (e.g., Ivanov

et al. 1997; Collins et al. 2004). It was not feasible for the numerical integrations to continue until the end of crater formation, and hence, we addressed the peak pressure and resultant particle velocity distributions at a given time. It has been shown that iSALE represents the maximum (peak) pressures experienced at each position in the targets caused by the shock wave well (Nagaki et al. 2016). The compression to a sufficient pressure by the shock wave and the release from the pressure by the rarefaction wave cause the fragmentation of the target material. Crater depth would correspond to a position experienced by a critical peak pressure value. On the other hand, crater diameter is directly related to fragmentation at the target surface, caused by a tensile phase due to the rarefaction wave (e.g., Melosh 1989). Since the rarefaction wave leads to upward motion of the target materials, the distribution of particle velocity near the surface should represent the extent of fragmentation near the surface. If the peak pressure and particle velocity distributions do not strongly depend on projectile shape and interior, the dimensions of the final crater are expected to be similar. To accurately reproduce the dependence of peak pressure distribution on projectile shape and interior in the simulation, we divided the wall thickness into 20 cells, resulting in > 160 cells per projectile radius for the three copper tubes. We inserted Lagrangian tracer particles into the computational cells and stored the maximum pressures experienced at a given time and temporal particle velocity in the simulations. The input parameters of the material models and calculation settings are summarized in Tables 2, 3, and 4.

Kadono *et al. Earth, Planets and Space*   (2022) 74:132

Page 7 of 12
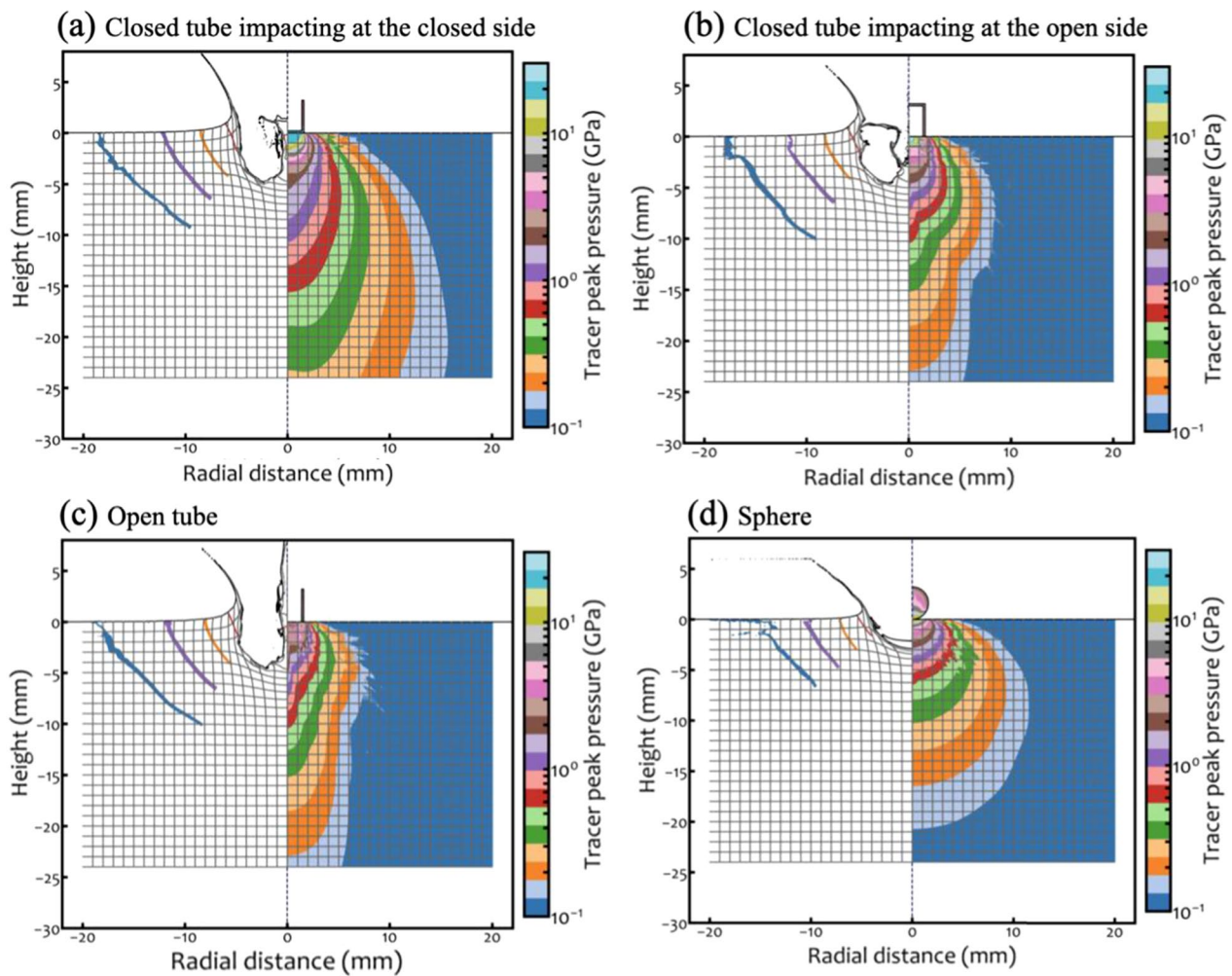
Fig. 5 Results of the numerical simulations for **a** a closed copper tube impacting at the closed side, **b** a closed copper tube impacting at the open side, **c** an open copper tube, and **d** a solid aluminum sphere. The projectile collides perpendicularly at the origin of the coordinate from the top. The right half shows the contour of the maximum (peak) pressures experienced. The left half shows the contour of the upward particle velocity; the blue, purple, orange, and red lines indicate 3, 10, 30, and 100 m/s, respectively

Figure 5 shows the results of the calculations: contours of the peak pressure experienced (right) and particle velocity (left). Note that we only used tracers with upward velocities in this plot (hereafter referred to as upward particle velocity). It appears that in any case, pressure decreases along the central axis in the same way, and that the contour lines of the upward particle velocity are distributed at a similar location. To evaluate the peak pressure and particle velocity more quantitatively, we obtained the profiles of the peak pressure and particle velocity along the central axis and target surface, respectively (the analyses are described in Additional file 1: S1 in detail). Figure 6 shows that the profiles of (a) peak pressure experienced and (b) particle velocity for the results shown in Fig. 5 along the central axis (Z-axis) and the target surface (R-axis), respectively (strictly a line 5

cells away from the Z and R axes; see the Additional file 1: S1). These show that the profile for each impact condition decreases with a similar slope at distances greater than projectile diameter D_p and that the difference between the profiles is within a factor of $\sim 2-3$. This implies that when projectile bulk density and impact velocity are the same, the pressure of shock wave detached from isobaric core is almost independent of the projectile shape and internal structure. Even if projectile has an internal structure (e.g., voids), since shock pressure is much higher than the strength of projectile, its shape and the internal structure are completely crushed, and the compressed density and average shock pressure are independent of initial shape and internal structure. Moreover, attenuation of detached shock waves depends on the geometrical

Kadono *et al. Earth, Planets and Space*   (2022) 74:132

Page 8 of 12
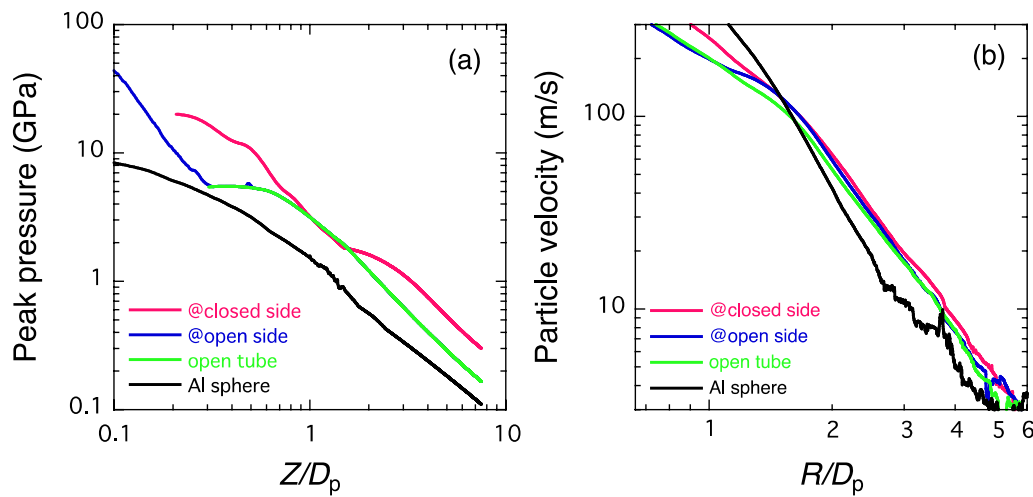
Fig. 6 Profiles of **a** peak pressure and **b** particle velocity along the central axis and the target surface, respectively, for the numerical results shown in Fig. 5. The profiles for the copper closed-tube projectile impacting at the open side and the open tube projectile are very similar and hence, the lines are almost overlapping

expansion of shock waves and elastic–plastic properties of target materials. Therefore, shock pressure and attenuation are independent of initial projectile structure. Thus, even if projectile shape and internal structure vary, the crater depth and diameter become almost the same when the bulk density and diameter of projectile and impact velocity are the same. Note that the profiles also show that the result for the aluminum solid projectile is similar to those for copper projectiles with internal structure. This suggests that even when projectiles are made of different materials, shock impedance becomes similar if bulk density is the same. More systematic investigation is necessary to understand why similar pressures are generated by porous projectiles with internal structure and solid projectiles of different materials when bulk density is the same.

We also simulated the impacts corresponding to the experiments with shot number 1031-2 (closed copper tube colliding at the closed end), 1031-3 (closed copper tube colliding at the open end), 0925-1 (open copper tube), and 1031-5 (solid aluminum sphere). The results are shown in Fig. 7a–d. The contours of the experienced peak pressure and particle velocity are shown on the right and left halves, respectively. For comparison, the crater profile in the corresponding experiment is overlaid (green curve). The shape of the cavity in the targets is very different from that of the final crater and does not become similar thereafter, although the size is comparable. It seems that it is still difficult to reproduce the exact shape of a crater in targets with strength. Figure 8 shows the profiles of (a) peak pressure experienced and

(b) particle velocity for the results shown in Fig. 7 along the central axis and target surface, respectively (strictly a line 5 cells away). The crater depth and radius normalized by D_p obtained in the experiments are also indicated. The peak pressure and particle velocity corresponding to the experimental results of crater depth and radius are shown in Fig. 9. The depth and radius of the final crater corresponded to ~ 2 GPa and ~ 10 m/s, respectively, in each case. In this figure, the results of the shot number 0925-2 and one of the shots in Dohi et al. (2012) (090528-1) are also plotted. (Note that the calculations for 0925-2 and 090528-1 in iSALE were conducted with low resolution and that nylon projectile was used in 090528-1. These calculations in iSALE with low resolution and nylon are described in Additional file 1: S2 and S3, respectively.) Even though the projectile density is different, the corresponding pressure is similar, and so is the corresponding particle velocity. The averages of the corresponding peak pressure and particle velocity are 1.9 ± 0.6 GPa and 13.0 ± 3.6 m/s, respectively. The compressive strength of basalt has been measured to be several hundred megapascals (e.g., Lockner 1995), which is slightly lower than the pressure corresponding to the crater depth. However, the compressive strength values were obtained using static compression tests, and the effect of strain rate could explain this difference (e.g., Kimberley et al. 2013). Therefore, the maximum depth of the final craters in the strength-dominated regime was determined by the balance between the intensity of the compressive pulse and the compressive strength of the target materials. On the other hand, the upward particle velocity u_p of ~ 10 m/s
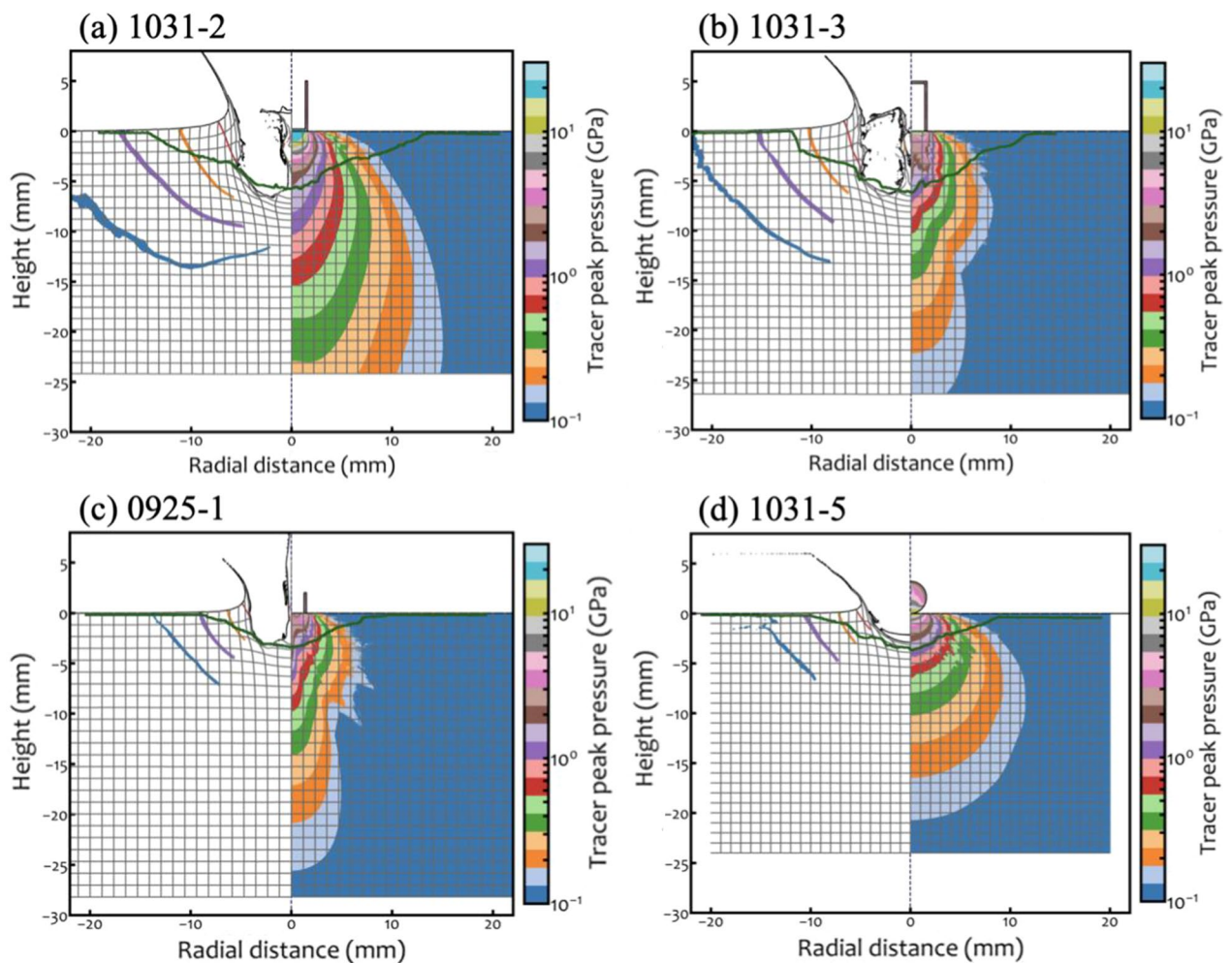
Fig. 7 Results of the numerical simulations corresponding the experiments of **a** a closed copper tube impacting at the closed side (1031-2), **b** a closed copper tube impacting at the open side (1031-3), **c** an open copper tube (0925-1), and **d** a solid aluminum sphere (1031-5). The right half shows the contour of the maximum (peak) pressures experienced. The left half shows the contour of the upward particle velocity; the blue, purple, orange, and red lines indicate 3, 10, 30, and 100 m/s, respectively. The crater profile in the experiment with the corresponding impact condition is shown for comparison (green curve)

corresponds to the tensile stress, T, of several tens of megapascals, which is estimated from $\delta_t C_0 u_p$, where δ_t and C_0 are the density and bulk sound velocity of basalt, 2.71 g/cm^3 (the average value for the targets in our experiments) and 2.60 km/s (e.g., Melosh 1989), respectively. This is similar to the tensile strength of basalt (e.g., Lockner 1995), suggesting that crater diameter is related to the tensile process. The results, namely, that crater depth and diameter are related to the compressive and tensile strengths of the targets, are consistent with our current understanding of the cratering process (e.g., Melosh 1989).

Summary

Crater formation experiments were conducted using projectiles of various shapes and basalt and porous gypsum targets. The surface (spall) diameter, inner (pit) diameter, and depth of the craters were measured. The surface diameter and depth for basalt and the pit diameter and depth for porous gypsum were scaled using pi-scaling law for crater formation in the strength regime, when using the bulk density of projectiles. Consequently, the result is the same as in the gravity regime. The numerical code iSALE was used to simulate the impact of projectiles of various shapes with similar bulk

Kadono *et al. Earth, Planets and Space* (2022) 74:132

Page 10 of 12
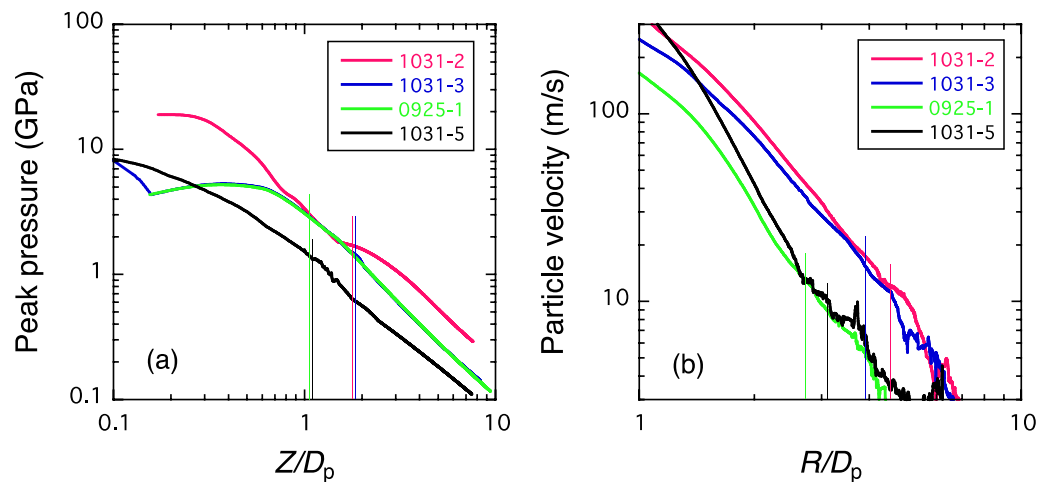
Fig. 8 Profiles of **a** peak pressure and **b** particle velocity along the central axis and the target surface, respectively, for the results shown in Fig. 7. The peak pressure profiles for 1031-3 (the closed tube impact at open side) and 0925-1 (open tube) are similar and hence almost overlap. The experimental results of crater depth and crater radius are indicated as vertical lines (the line and profile with the same color are corresponding)

densities. The contours of the maximum pressure experienced and the particle velocity in the targets obtained by the calculations were similar regardless of the projectile shape and interior. This implies that the dimensions of final craters were almost identical and are consistent with the experimental results. Thus, we conclude that the size of the crater formed by the impact of projectiles with different shape and interior structure can be scaled using a conventional scaling law in the strength regime, when the bulk density is set as the projectile density. Note that despite varied projectile shape and interior structure, the aspect ratio of projectiles used in this study was approximately 1. If the aspect ratio is larger, the conventional laws may not be able to explain crater sizes.

When new exploration methods, such as SCI-type impact experiments, are to be used in future missions to investigate the properties of the object being explored (e.g., the strength of boulders), the results of our study should provide constraints on the design of an impactor.

Supplementary Information

> **Additional file 1.** Supporting materials for numerical simulations. Section S1. Analyses to obtain the profiles of peak pressure and particle velocity. Section S2. Procedure for low resolution calculations. Section S3. Equation of state for Nylon 66.

Author contributions
TK, MA, ST, MY, SH, KS, CO, KO, YI, and KW conducted the impact experiments and contributed to data preparation, interpretation of results, and writing of
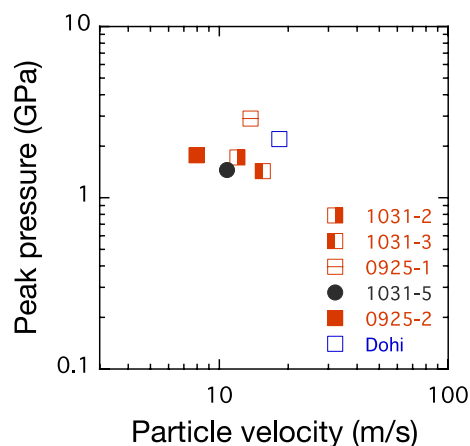
Fig. 9 Peak pressure and particle velocity corresponding to the experimental results of crater depth and radius. The results of 0925-2 and one of the shots in Dohi et al. (2012) (090528-1) are also plotted

Kadono *et al. Earth, Planets and Space* (2022) 74:132

Page 11 of 12

the manuscript. KK and YS performed the numerical simulations, and drafted the initial manuscript. TK designed the paper and completed the manuscript. All the authors read and approved the final manuscript.

Declarations

Author details
[1]Department of Basic Sciences, University of Occupational and Environmental Health, Kitakyushu, Japan. [2]Department of Planetology, Kobe University, Kobe, Japan. [3]Institute of Space and Astronautical Science, Japan Aerospace Exploration Agency, Sagamihara, Japan. [4]Planetary Exploration Research Center, Chiba Institute of Technology, Narashino, Japan. [5]JAXA Space Exploration Center, Japan Aerospace Exploration Agency, Sagamihara, Japan.

References

A'Hearn MF et al (2005) Deep impact: excavating comet Tempel 1. Science 310:258–264

Amsden A, Ruppel H, Hirt C (1980) SALE: a simplified ALE computer program for fluid flow at all speeds. Los Alamos National Laboratories Report LA-8095:101p

Arakawa M et al (2020) An artificial impact on the asteroid (162173) Ryugu formed a crater in the gravity-dominated regime. Science 368:67–71

Bowling TJ, Johnson BC, Wiggins SE, Walton EL, Melosh HJ, Sharp TG (2020) Dwell time at high pressure of meteorites during impact ejection from Mars. Icarus 343:113689

Colaprete A et al (2010) Detection of water in the LCROSS ejecta plume. Science 330:463–468

Collins GS, Melosh HJ, Ivanov BA (2004) Modeling damage and deformation in impact simulations. Met Planet Sci 39:217–231

Collins GS, Elbeshausen D, Davison TM, Wunnemann K, Ivanov B, Melosh HJ (2016) iSALE-Dellen manual. Figshare. https://doi.org/10.6084/m9.figshare.3473690.v2

Dohi K, Arakawa M, Okamoto C, Hasegawa S, Yasui M (2012) The effect of a thin weak layer covering a basalt block on the impact cratering process. Icarus 218:751–759

Drucker DC, Prager W (1952) Soil mechanics and plastic analysis or limit design. Q Appl Math 10:157–165

Gault DE, Heitowit ED (1963) The partition of energy for hypervelocity impact craters formed in rock. Proc Sixth Hypervelocity Impact Symp 2:419–456

Hänström A, Lazor P (2000) High pressure melting and equation of state of aluminum. J Alloy Compd 305:209–215

Hermalyn B, Schultz PH, Shirley M, Ennico K, Colaprete A (2012) Ejecta dynamics and the LCROSS impact event. Icarus 218:654–665

Holsapple KA (1993) The scaling of impact processes in planetary sciences. Annu Rev Earth Planet Sci 21:333–373

Housen KR, Holsapple KA (2011) Ejecta from impact craters. Icarus 211:856–875

Ivanov BA, Deniem D, Neukum G (1997) Implementation of dynamic strength models into 2-D hydrocodes: applications for atmospheric breakup and impact cratering. Int J Impact Eng 20:411–430

Johnson GR, Cook WH (1983) A constitutive model and date for metals subjected to large strains, high strain rates and high temperatures. In: Seventh international symposium on Ballistics, Hague

Japel S, Boehler R, Ross M (2005) Melting of copper and nickel at high pressure: the role of d-electrons. Phys Rev Lett 95:167801

Kadono T, et al. (2020) Impact experiment on asteroid (162173) Ryugu: Structure beneath the impact point revealed by in situ observations of the ejecta curtain. ApJ Letters 899: L22

Kadono T, Sugita S, Sako S, Ootsubo T, Honda M, Kawakita H, Miyata T, Furusho R, Watanabe J (2007) The thickness and formation age of the surface layer on comet 9P/Tempel 1. Astrophys J Lett 661:L89–L92

Kadono T, Niimi R, Okudaira K, Hasegawa S, Tabata M, Tuchiyama A (2012) Penetration into low-density media: in situ observation of penetration process of various projectiles. Icarus 221:587–592

Kadono T, Suzuki AI, Araki S, Asada T, Suetsugu R, Hasegawa S (2018) Investigation of impact craters on flat surface of cylindrical targets based on experiments and numerical simulations. Planet Space Sci 163:77–82

Kawai N, Tsurui K, Hasegawa S, Sato E (2010) Single microparticle launching method using two-stage light-gas gun for simulating hypervelocity impacts of micrometeoroids and space debris. Rev Sci Instrum 81:115105. https://doi.org/10.1063/1.3498896

Kimberley J, Ramesh KT, Daphalapurkar NP (2013) A scaling law for the dynamic strength of brittle solids. Acta Mater 61:3509–3521

Köster W, Franz H (1961) Poisson's ratio for metals and alloys. Metall Rev 6:1–56

Lockner DA (1995) Rock failure. In: Ahrens TJ (ed) Rock physics and phase relations: a handbook of physical constants, AGU Reference Shelf 3. American Geophysical Union, Washington DC, pp 128–148

Love SG, Hörz F, Brownlee DE (1993) Target porosity effects in impact cratering and collisional disruption. Icarus 105:216–224

Lundborg N (1968) Strength of rock-like materials. Int J Rock Mech Min Sci 5:427–454. https://doi.org/10.1016/0148-9062(68)90046-6

Melosh HJ (1989) Impact cratering: a geologic process. Oxford University Press, New York

Melosh HJ, Ryan EV, Asphaug E (1992) Dynamic fragmentation in impacts: hydrocode simulation of laboratory impacts. J Geophys Res 97:14735–14759

Nagaki K, Kadono T, Sakaiya T, Kondo T, Kurosawa K, Hironaka Y, Shigemori K, Arakawa M (2016) Recovery of entire shocked samples in a range of pressure from ~100 GPa to Hugoniot elastic limit. Meteorit Planet Sci 51:1153–1162

Nakamura AM, Patrick M, Setoh M (2007) Weibull parameters of Yakuno basalt targets used in documented high-velocity impact experiments. J Geophys Res 112:E02001. https://doi.org/10.1029/2006JE002757

Pierazzo E, Artemieva NA, Ivanov BA (2005) Starting conditions for hydrothermal systems underneath Martian craters: Hydrocode modeling. In: Kenkmann T, Horz F, Deutsch A (ed) Large Meteorite Impacts, Spec Pap Geol Soc Am 384: 443–457

Pierazzo E et al (2008) Validation of numerical codes for impact and explosion cratering: impacts on strengthless and metal targets. Meteorit Planet Sci 43:1917–1938

Poirier JP (1991) Introduction to the physics of the earth's interior. Cambridge University Press, New York

Saiki T, Imamura H, Arakawa M, Wada K, Takagi Y, Hayakawa M, Shirai K, Yano H, Okamoto C (2017) The small carry-on impactor (SCI) and the Hayabusa2 impact experiment. Space Sci Rev 208:165–186

Sato M, Kurosawa K, Kato S, Ushioda M, Hasegawa S (2021) Shock remanent magnetization intensity and stability distributions of single-domain titanomagnetite-bearing basalt sample under the pressure range of 0.1–10 GPa. Geophys Res Lett 48:e2021GL092716

Schultz PH, Gault DE (1985) Clustered impacts: experiments and implications. J Geophys Res 90:3701–3732

Schultz PH, Hermalyn B, Colaprete A, Ennico K, Shirley M, Marshall WS (2010) The LCROSS cratering experiment. Science 330:468–472

Sugita S et al (2005) Subaru telescope observations of deep impact. Science 310:274–278

Suzuki AI, Okamoto C, Kurosawa K, Kadono T, Hasegawa S, Hirai T (2018) Increase in cratering efficiency with target curvature in strength-controlled crater. Icarus 301:1–8

Thompson SL, Lauson HS (1972) Improvements in the Chart-D radiation hydrodynamic code III: revised analytical equation of state. Sandia Laboratories, Albuquerque, NM. pp SC-RR-71 0714 119 pp

Tillotson JH (1962) Metallic equations of state for hypervelocity impact. Technical Report GA-3216 general atomic report

Kadono *et al. Earth, Planets and Space*   (2022) 74:132

Page 12 of 12

Wünnemann K, Collins GS, Melosh HJ (2006) A strain-based porosity model for use in hydrocode simulations of impacts and implications for transient crater growth in porous targets. Icarus 180:514–527

Wünnemann K, Collins GS, Osinski GR (2008) Numerical modelling of impact melt production in porous rocks. Earth Planet Sci Lett 269:530–539

Yasui M, Arakawa M, Hasegawa S, Fuita Y, Kadono T (2012) In situ flash X-ray observation of projectile penetration processes and crater cavity growth in porous gypsum target analogous to low-density asteroids. Icarus 221:646–657

Publisher's Note